Supplementary Information for

Synergistic Cu nanoparticle-single atoms leveraging hydrogen spillover for selective CO electroreduction to acetate

Qinglong Wang,[a,b] Tianfu Liu,*[a,d] Xinhui Guo,[a,d] Pengfei Wei,[a,c] Dunfeng Gao,*[a,d] Guoxiong Wang [a,c] and Xinhe Bao [a,c,d]

[a]State Key Laboratory of Catalysis, Dalian Institute of Chemical Physics, Chinese Academy of Sciences, Dalian 116023, China

[b]Key Laboratory of Green Chemical Process of Ministry of Education, Hubei Key Laboratory of Novel Reactor and Green Chemical Technology, School of Chemical Engineering and Pharmacy, Wuhan Institute of Technology, Wuhan 430205, China

[c]Department of Chemistry, Shanghai Key Laboratory of Molecular Catalysis and Innovative Materials, iChEM (Collaborative Innovation Center of Chemistry for Energy Materials), Fudan University, Shanghai 200438, China

[d]University of Chinese Academy of Sciences, Beijing 100049, China

Corresponding authors: ltianfu@dicp.ac.cn; dfgao@dicp.ac.cn

Experimental Section

Chemicals

2,6-diacetylpyridine (≥99%), 1,8-diaminonaphthalene (≥97%), copper nanoparticles (Cu, 25 nm) were purchased from Shanghai Aladdin Biochemical Technology Co., Ltd. Copper (II) chloride dihydrate ($CuCl_2·2H_2O$, ≥99.0 wt%) was purchased from Tianjin Kemiou Chemical Reagent Co., Ltd. Potassium hydroxide (KOH, 95 wt%) and Cu foil (99.99 wt%) were all purchased from Macklin Co., Ltd. Copper phthalocyanine (CuPc, 97%), sodium borohydride ($NaBH_4$, 96%) and anhydrous ethanol (C_2H_5OH, >99%) were purchased from Sinopharm Chemical Reagent Co., Ltd. Carbon black (Vulcan XC-72R) was purchased from Cabot Corporation. Nafion 520 ionomer (~5 wt% in a mixture of lower aliphatic alcohols and water) was purchased from DuPont.

Synthesis of Cu_{NP}-Cu_1, 0.5 Cu_{NP}-Cu_1 and 2Cu_{NP}-Cu_1 catalysts

0.41g 2,6-diacetylpyridine (DAP) and 0.44g 1,8-diaminonaphthalene (DAN) with a molar ratio of 2 were dissolved in 55 mL of ethanol (0.82g DAP and 0.88g DAN for 0.5Cu_{NP}-Cu_1). After complete dissolution, 0.1 g of oxalic acid was added to initiate the polymerization of DAP and DAN. The solution was stirred for 4 hours, followed by the dropwise addition of a 0.65 mmol $CuCl_2·2H_2O$-ethanol solution (1.3 mmol $CuCl_2·2H_2O$ for 2Cu_{NP}-Cu_1). After reacting for 12 hours, the resulting product was centrifuged, washed, and dried to obtain a gray-black catalyst precursor powder. This precursor was then annealed under an Ar atmosphere at heating rates of 5°C min^{-1} to temperatures of 450℃ and 700°C for 1 hour, respectively.

Synthesis of Cu NPs

A solution of 17.2 mg $CuCl_2·H_2O$ in 10 mL acetone was dispersed in 200 mL of ethylene glycol monoethyl ether. 100 mg of carbon black (XC72R) were added to this solution and ultrasonicated for dispersion. After stirring for 10 hours, a sodium borohydride solution (10 mL, 2.7 M) was added dropwise. Following a 5-minute reaction, the product was centrifuged, washed, and dried to obtain Cu NPs. This powder was then heated to 300°C at a rate of 3°C min^{-1} in a 5% H_2/Ar gas mixture and held at this temperature for 3 hours to produce Cu NPs.

Synthesis of CuSA, 2CuSA and 0.5CuSA catalysts

One hundred milligrams of Cu_{NP}-Cu_1 powder were added to 20 mL of 4 M H_2SO_4 solution and sonicated for 30 minutes. The dispersion was then placed in a constant temperature oil bath at 85°C with magnetic stirring for 10 hours to etch the Cu NPs. After confirming complete etching of Cu NPs, the suspension was washed and centrifuged until neutral pH. The dried powder was annealed at 700°C for 1 hour under an Ar atmosphere. The sample was labeled as CuSA.

2CuSA and 0.5CuSA catalysts were synthesized following the same procedures as illustrated above by acid etching $2Cu_{NP}$-Cu_1 and $0.5Cu_{NP}$-Cu_1 to remove Cu NPs.

Electrode preparation

Cathode: A dispersion containing the catalyst and D520 (mass ratio 9:1) in ethanol was drop-coated onto a gas diffusion electrode, yielding a catalyst loading of 0.5 mg cm^{-2}.

Anode: The anode catalyst layer was fabricated by drop-coating a dispersion of commercial iridium black catalyst and D520 (mass ratio 9:1) in ethanol onto titanium felt, achieving an Ir black loading of 1.0 mg cm^{-2}.

Electrochemical CO reduction

The CO reduction reaction (CORR) was conducted in flow cell. During testing, the potential is controlled using an electrochemical workstation to perform chronoamperometry. The electrochemical workstation model used is the Agilent 8860 GC System. The active electrode areas for both the cathode and anode are 2 cm^2. The cathode electrode is a gas diffusion electrode (GDE), while the anode is a titanium foam coated with Ir black. The reference electrode is an Ag/AgCl electrode. All potentials were referenced to reversible hydrogen electrode (RHE) and corrected by *i*R compensation according to the formula: E (RHE) = E (Ag/AgCl) + 0.21 V + 0.0591 × pH – *i*R × 85%. Electrochemical surface area (ECSA) was obtained by conducting cyclic voltammetry (CV) with the scan rates from 40 to 120 mV s^{-1}. The current density differences ($\Delta j = j_a - j_c$)/2 were plotted against scan rates, and the slopes were used to derive C_{dl}. Electrochemical impedance spectroscopy (EIS) measurements were counducted at open-circuit voltage in the frequency range of 10^5 ~ 10^{-2} Hz with a

perturbation of 5 mV.

Products analysis

Gas chromatography analysis: The gas chromatograph was calibrated using a standard gas of known composition prior to analysis, with correction factors relative to N_2 calculated for each component. During testing, product concentrations were determined from measured peak areas. Faradaic efficiencies for the various products were then calculated based on the moles of product derived from these peak areas and the total moles of electrons supplied, determined from the applied current and time.

Liquid product analysis: Liquid products were analyzed using a Bruker AVANCE III 400 MHz NMR spectrometer. Standard curves for target products were generated using solutions of known concentrations. 6 mM 3-(trimethylsilyl)-1-propanesulfonic acid sodium salt (DSS) was used as an internal standard. Product concentrations were calculated from the peak areas obtained in the sample NMR spectra.

The Faradaic efficiency of a specific product is calculated as follows:

$$\varepsilon_{\text{Faradaic,i}} = Q_i/Q_{\text{total}} \times 100 = (N_i \times n_i \times \text{F})/Q_{\text{total}} \times 100$$

where,

$\varepsilon_{\text{Faradaic,I}}$ represents the Faradaic efficiency of product *i*, %;

Q_i represents the charge used for the production of the product *i*, C;

Q_{total} represents the consumed charge, C;

N_i represents the amount of the product *i*, mol;

n_i represents the number of electrons transferred to form the product *i*;

F is Faraday constant, which is 96485 C mol^{-1}.

The carbon selectivity (Sel.) for the formation of a specific product *i* is defined as follows:

$$\text{Sel.}i\ (\%) = x_i r_i/(r_{\text{methane}} + 2r_{\text{ethlene}} + 2r_{\text{acetate}} + 2r_{\text{ethanol}} + 3r_{\text{n-propanol}})$$

x_i: the carbon number of a specific product *i*;

r_i: is the production rate of a specific product *i*.

Kinetic isotope effect (KIE) experiments

KIE test was conducted using an H-cell electrolyzer. A 100 mL reagent bottle served as both the electrolyte reservoir and gas-liquid separation chamber, sealed with a plastic three-hole feeding cap. The peristaltic pump was used for recycling electrolyte. After reacting for a specified duration, gaseous products were quantified via gas chromatography. The reaction was then terminated, and liquid products were collected for NMR analysis.

Using deuterated DMSO (DMSO-d6) as an internal standard, standard solutions were prepared according to the ratios of DMSO-d6 and D_2O specified in Fig. S17. Deuterium lock mode NMR was employed to analyze deuterated acetate (acetate-d) and DMSO-d6. The peak area ratios were calculated to establish a linear equation correlating amount of substance $n_{acetate}$ and $S_{acetate\text{-}d}$ ($NMR_{acetate}/NMR_{DMSO\text{-}d6}$). This linear equation was subsequently applied to determine the concentration of liquid products in the kinetic isotope effect experiment.

Catalyst characterization

Catalyst morphology was analyzed using a field emission scanning electron microscope (FESEM, Quanta 200F). Transmission electron microscopy (TEM) and energy-dispersive X-ray spectroscopy (EDS) elemental mapping were performed on a JEM-2100 microscope operated at 200 kV. Atomic-level metal distribution was characterized using high-angle annular dark-field scanning transmission electron microscopy (HAADF-STEM, JEM-ARM300F). Powder XRD patterns were recorded on a PANalytical X'pert PRO diffractometer using Cu Kα radiation (40 kV, 40 mA) with a scan rate of 5° min^{-1}. XPS measurements were conducted on a Thermo Scientific ESCALAB 250Xi spectrometer. All binding energies were referenced to the C 1s peak at 284.8 eV. Cu K-edge (E_0 = 8979 eV) XAS spectra were collected at the BL14W1 beamline of the Shanghai Synchrotron Radiation Facility (SSRF) in fluorescence-yield mode. Metallic Cu foil was used as an energy reference for calibration. Data processing (baseline subtraction, normalization) was performed using the IFEFFIT package (ATHENA, ARTEMIS), yielding normalized absorbance spectra. Fourier-transformed extended X-ray absorption fine structure (FT-EXAFS) data were fitted using a metallic Cu model for Cu-Cu contributions. In situ Raman spectra of electrodes were acquired

using a Renishaw inVia microscope equipped with a 532 nm laser and a 50× long-working-distance objective lens (Leica). Measurements employed a custom electrochemical cell with a membrane-electrode assembly (MEA) configuration. The anode and anion exchange membrane matched those used in the actual CORR experiments. The cathode catalyst layer was prepared by spraying catalyst ink (using Nafion ionomer solution as binder) directly onto the membrane. Electrolysis was performed at various current densities for 10 minutes prior to spectral acquisition. Inductively coupled plasma-optical emission spectrometry (ICP-OES) measurements were conducted using an ICP-OES 7300DV system.

Double layer capacitance measurements

The electrochemical active surface area (ECSA) is proportional to the double-layer capacitance (C_{dl}). The C_{dl} was determined by measuring the capacitive current associated with double-layer charging from the scan-rate dependence of cyclic voltammograms (CVs). Measurements were conducted in a flow cell using 1.0 M KOH aqueous electrolyte. An Ag/AgCl electrode and an Ir black electrode served as the reference and counter electrodes, respectively. CVs were recorded at scan rates of 40, 60, 80, 100, and 120 mV s^{-1} within a non-faradaic potential window.

CO stripping test

CO stripping voltammetry was performed in a flow cell using a three-electrode configuration. The working electrode was prepared as follows: 0.5 mg of catalyst was dispersed in 5 mL of ethanol containing 10 µL of 5 wt% Nafion D520 dispersion to form a homogeneous ink. This ink was then uniformly spread onto a 1 cm^2 carbon paper and dried at room temperature. An Ag/AgCl electrode and an Ir black electrode served as the reference and counter electrodes, respectively. The electrolyte was 0.2 M K_2SO_4 aqueous solution. Prior to measurement, CO was adsorbed onto the catalyst surface by holding the working electrode at –1.2 V vs. Ag/AgCl while bubbling CO through the electrolyte for 10 minutes, followed by Ar purging for an additional 10 minutes to remove residual dissolved CO. Subsequently, cyclic voltammetry scans were conducted from –0.8 V to 0 V at a scan rate of 50 mV s^{-1}.

Density functional theory (DFT) calculations

DFT calculations and ab initio molecular dynamics (AIMD) theoretical calculations were performed using the Vienna Ab-initio Simulation Package (VASP) with the projector augmented-wave (PAW) pseudo-potential [1, 2]. All calculations employed the Perdew-Burke-Ernzerhof (PBE) exchange-correlation functional within the generalized gradient approximation (GGA) and a plane-wave cutoff energy of 400 eV [3, 4]. DFT-D3 method of Grimme was used to calculate the van der Waals correction for DFT calculations [5]. All structures were optimized until the atomic forces were smaller than 0.05 eV $Å^{-1}$ and spin-polarization was considered in all the calculations. The computational hydrogen electrode (CHE) model proposed by Nørskov et al. was applied to investigate the *COCOH formation energy [6]. In CHE method, the relative free energy change is calculated as:

$$\Delta G = \mu[\text{product}] - \mu[\text{reactant}] - 0.5\mu[H_2\ (g)] + eU$$

Where μ is the chemical potential and U is the applied electrical potential. Therefore, in the step involving proton-electron transfer, $\Delta G(U) = \Delta G_0(U) + eU$, where U is the potential versus the reversible hydrogen electrode, ΔG_0 is the free energy at U = 0 V.

The Gibbs free energy (G) is calculated with following equation.

$$G = E_{\text{Total}} + ZPE - TS + \int C_p dT$$

Where E_{Total} is the total electronic energy, ZPE, S and $\int C_p dT$ are the zero-point vibrational energy, entropy and heat capacity at 298.15 K and 1 atm, respectively.

The Cu(100) and Cu-N_3 surfaces were modeled using four layer slabs to study H_2O dissociation, and Cu(111) was selected to study the formation of *COCOH and *CCO. A vacuum region of at least 15 Å between any two repeated slabs was used to avoid interactions between repeated slabs along z-direction for DFT calculations. The Brillouin zone was sampled with a gamma k point grid mesh. For Cu model, the top two layers and the adsorbates were fully relaxed, and the remaining layers were fixed.

The model for Cu-N_3 is composed of 66 carbon, 3 nitrogen and 1 Cu atoms. The cell has lattice lengths a = b =14.81 Å, c =20 Å, with angles α = β = 90°, γ =120°. A total of 87 H_2O molecules were added to fill the vacuum of the slab of Cu-N-C with a density of water of approximately of 1g cm^{-3}. The Cu model consists of 72 hydrogen, 36

oxygen, and 27 copper atoms. The periodic unit cell is defined with lattice parameters $a = b = 7.668$ Å, $c = 27.03$ Å and angles $\alpha = \beta = \gamma = 90°$, forming an orthorhombic box. A total of 36 H_2O molecules were included to fill the vacuum region above the Cu surface to maintain the density of water. The canonical (NVT) ensemble used Nose-Hoover thermostats at 298.15 K to sample the MD simulations [7, 8]. The models are equilibrated for runtimes of at least 5 ps with time step of 1.0 fs. For H_2O dissociation, constrained MD was carried out by combining slow-growth and blue-moon sampling techniques [9]. The difference between the distance from the one H atom in H_2O to oxygen in H_2O and the distance from the H to N site in Cu catalyst is chosen as the collective variable (CV). In this approach, the system is driven along the CV at a constant pulling rate, and the irreversible work associated with the transformation from state (1) to state (2) is calculated as:

$$\Delta A_{1\to 2} = \int_{\xi(1)}^{\xi(2)} \left(\frac{\partial \mathrm{V(q)}}{\partial \xi}\right) \cdot \dot{\xi} dt$$

$$\omega_{1\to 2}^{\mathrm{irrev}} = \int_{0}^{T} \left(\frac{\partial V(q(t))}{\partial \xi(t)}\right) \dot{\xi}(t) dt$$

Where *V(q)* is the potential energy of the system as a function of atomic coordinates q, and $\xi(t)$ is the time dependent CV. The quantity $\frac{\partial(\mathrm{V})}{\partial \xi}$ corresponds to the generalized force conjugate to the CV. In the quasi-static limit, where the system is driven infinitely slowly and remains in equilibrium throughout the transformation, the irreversible work converges to the true Helmholtz free energy difference:

$$\Delta A_{1\to 2} = \lim_{\dot{\xi}\to 0} \omega_{1\to 2}^{\mathrm{irrev}}$$

This method enables the estimation of free energy changes along a reaction coordinate without requiring explicit thermodynamic integration or enhanced sampling techniques, although sufficient sampling and a sufficiently slow pulling rate are required to reduce dissipative effects and obtain accurate results [10]. The process is set to be driven by a CV increase of 0.0002 Å fs^{-1}.

Supplementary Fig.s and Tables

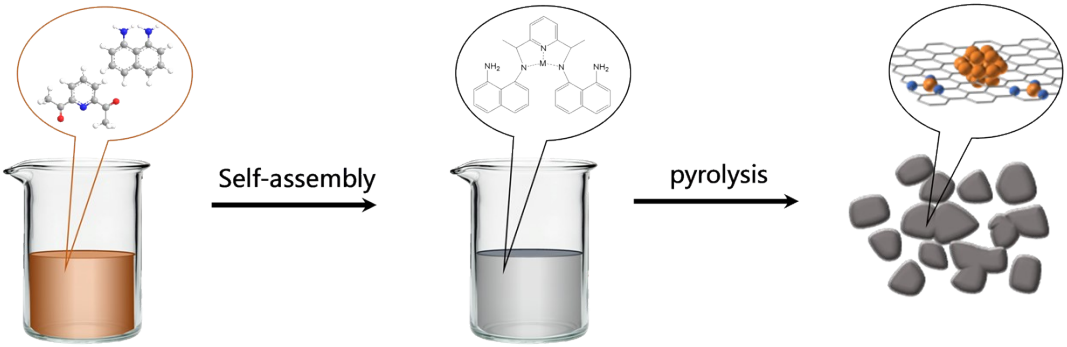

Fig. S1. Schematic illustration of the synthesis of Cu_{NP}-Cu_1 catalyst.

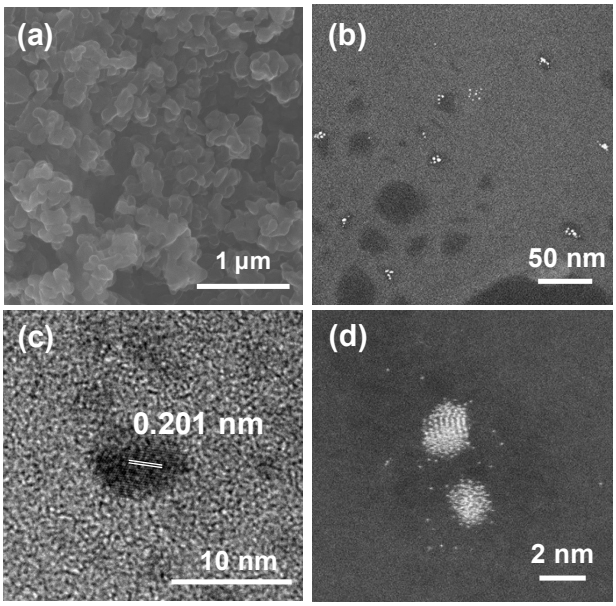

Fig. S2. (a) SEM image and (b, c) TEM images of Cu_{NP}-Cu_1 catalyst, (d) Aberration-corrected HAADF-STEM image of Cu_{NP}-Cu_1 catalyst.

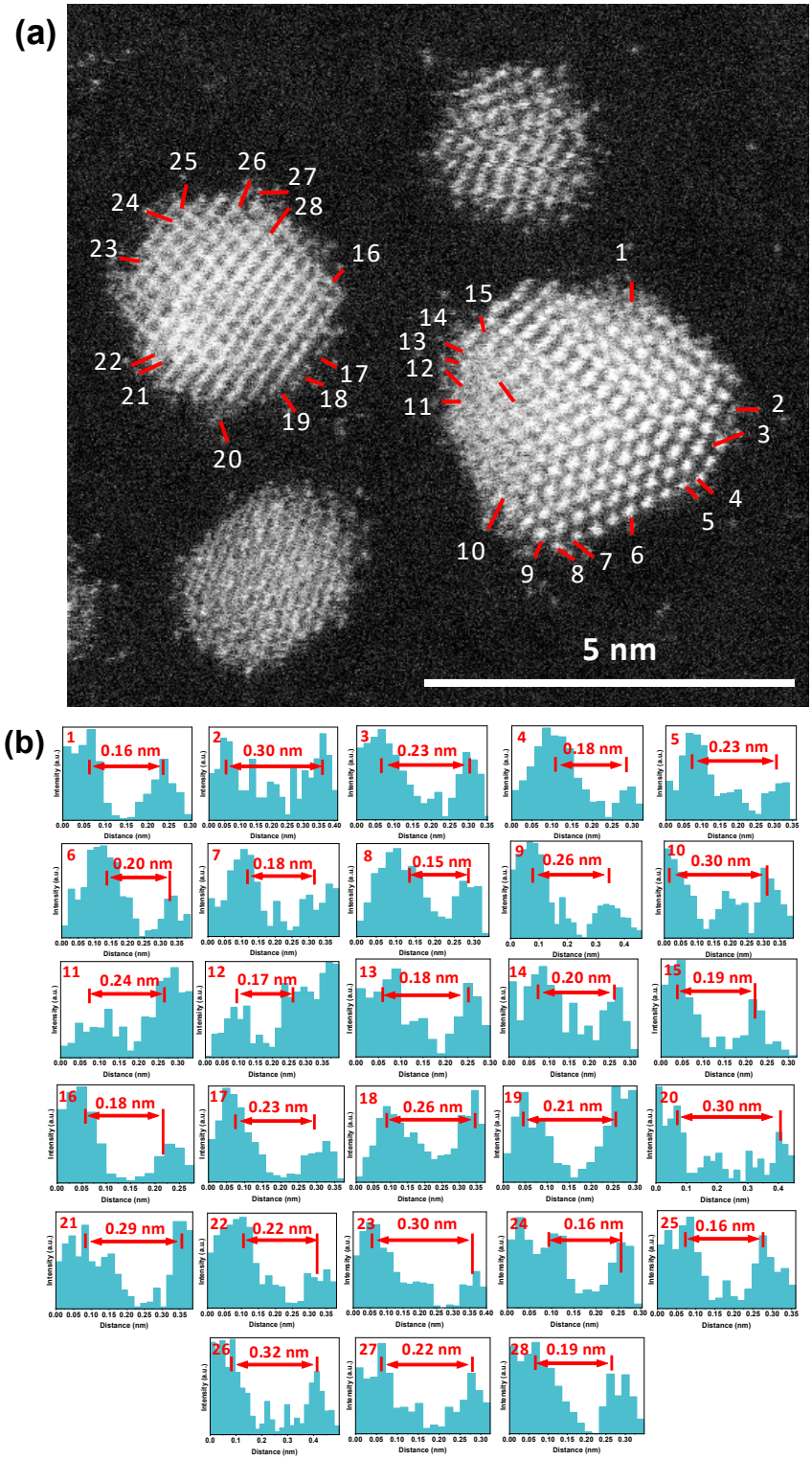

Fig. S3. (a) AC-HAADF-STEM image of Cu_{NP}-Cu_1 in Fig. 1c. (b) Extracted line profile along red direction in (a). The numbers represent the location of red line.

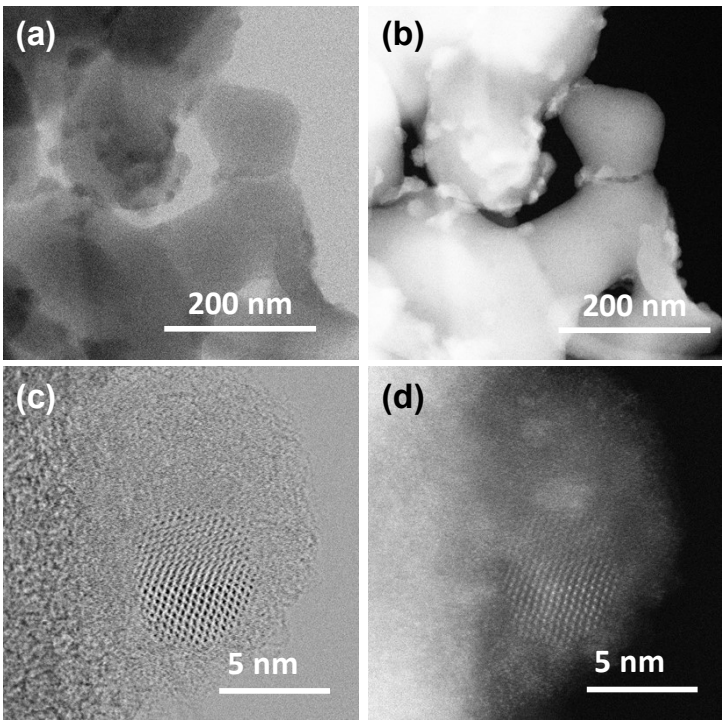

Fig. S4. (a, c) Aberration-corrected STEM images of $2Cu_{NP}$-Cu_1 catalyst. (b, d) Aberration-corrected HAADF-STEM images of (a, c).

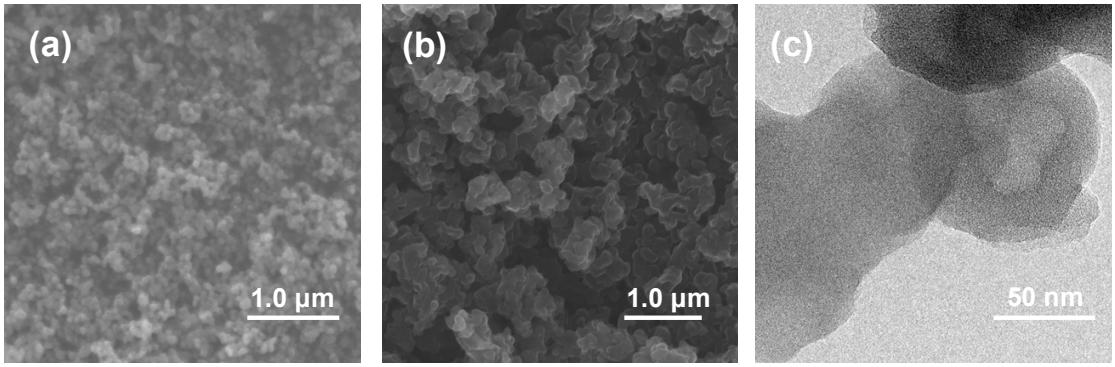

Fig. S5. SEM images of (a) Cu NPs, and (b) CuSA. (c) TEM image of CuSA.

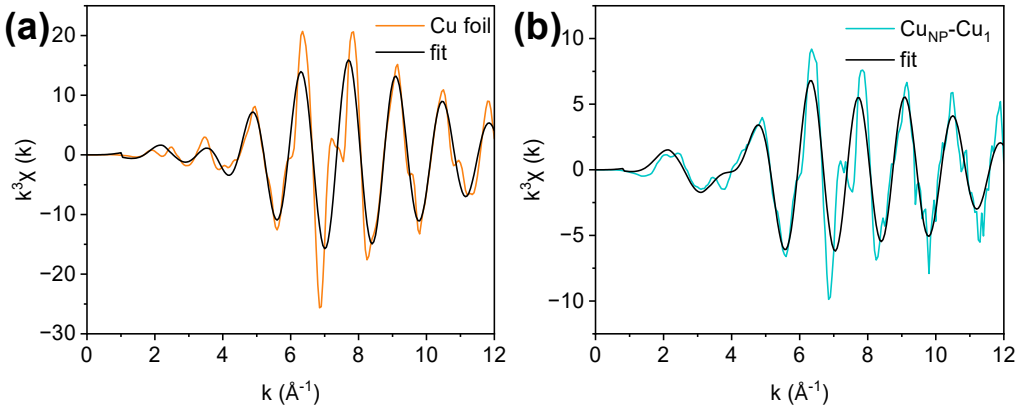

Fig. S6. The k^3-weighted Cu K-edge EXAFS spectra of (a) Cu foil, (b) Cu_{NP}-Cu_1.

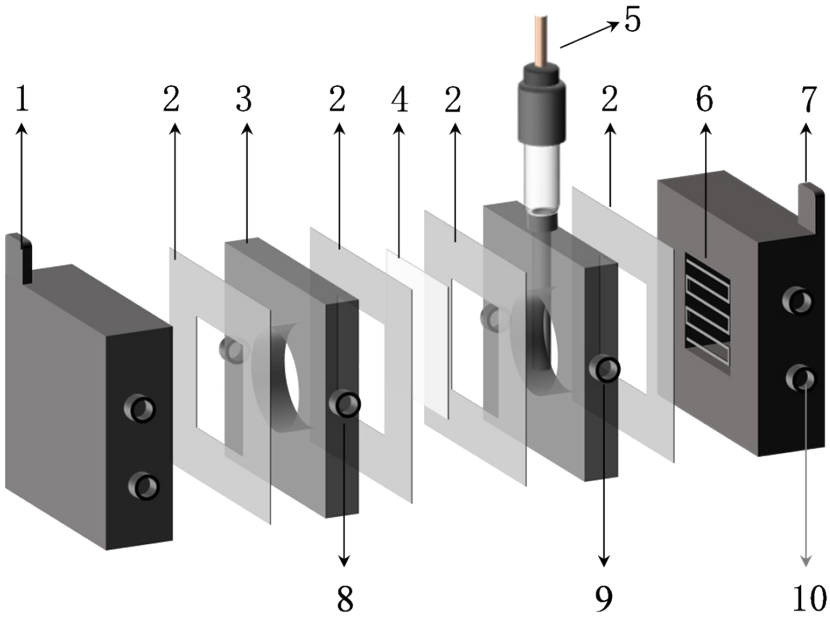

Fig. S7. Schematic diagram of flow cell for CORR. 1, anode. 2, silastic gasket. 3, acrylic board of anode. 4, anion-exchange membrane. 5, reference electrode. 6, flow field of cathode. 7, cathode. 8, electrolyte inlet/outlet of anode. 9, electrolyte inlet/outlet of cathode. 10, CO inlet.

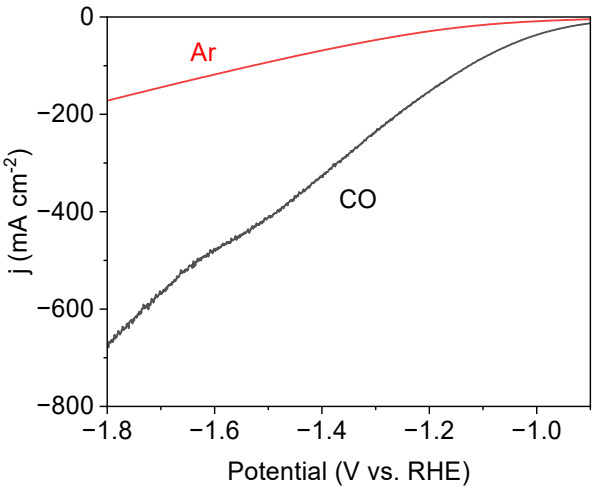

Fig. S8. LSV curves of Cu_{NP}-Cu_1 catalyst in CO or Ar atmosphere.

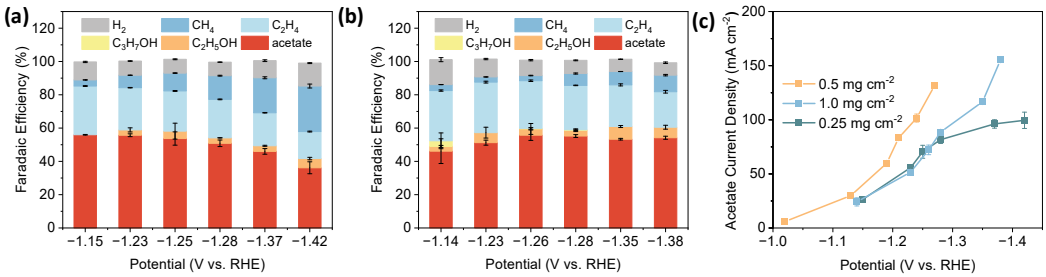

Fig. S9. Faradaic efficiency of products for Cu_{NP}-Cu_1 loading: (a) 0.25 mg cm^{-2} and (b) 1 mg cm^{-2}. (c) Acetate current densities as a function of potential over different mass loading of catalyst.

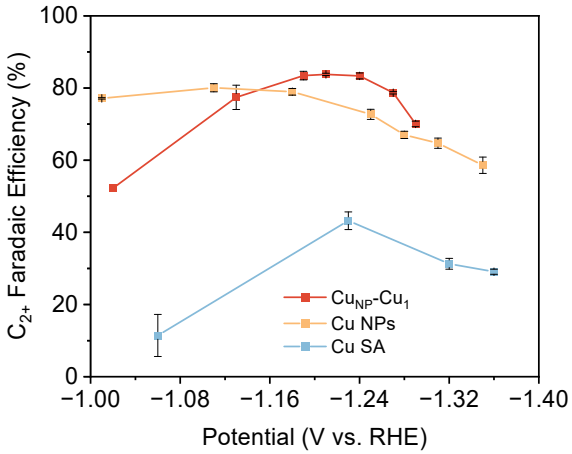

Fig. S10. The C_{2+} Faradaic efficiency at different potentials over Cu_{NP}-Cu_1, Cu NPs and CuSA catalyst in 1.0 M KOH electrolyte.

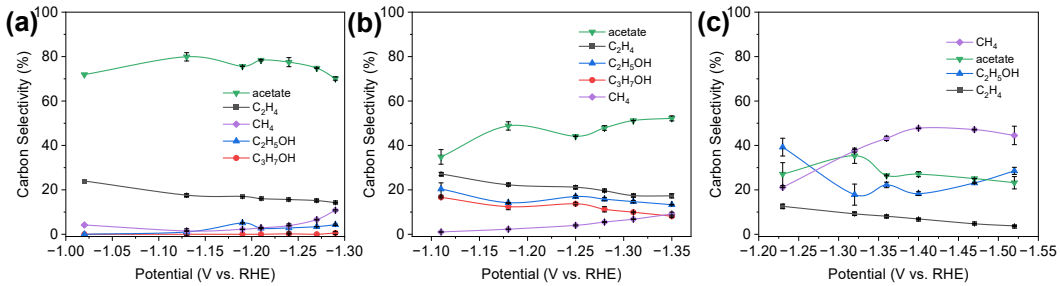

Fig. S11. Potential-dependent carbon selectivity of CO electrolysis products over (a) Cu_{NP}-Cu_1, (b) Cu NPs and (c) CuSA catalyst in 1.0 M KOH electrolyte.

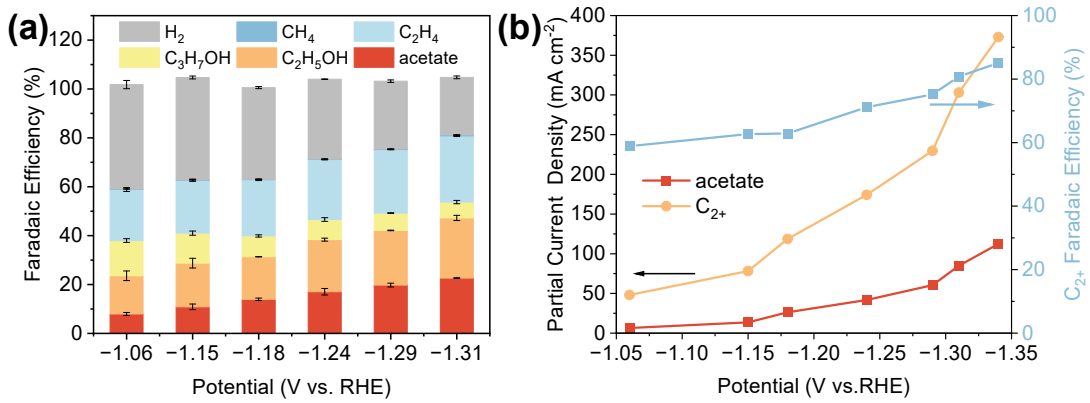

Fig. S12. (a) Faradaic efficiency of products for commercial Cu (25 nm). (b) The C_{2+}/acetate partial current density and Faradaic efficiency of C_{2+} products at different potentials over commercial Cu (25 nm) in 1.0 M KOH electrolyte.

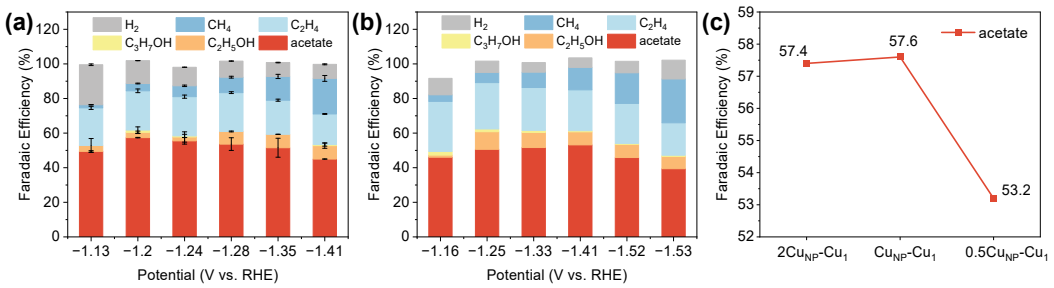

Fig. S13. Faradaic efficiency of products over (a) $2Cu_{NP}$-Cu_1, and (b) $0.5Cu_{NP}$-Cu_1 in 1.0 M KOH electrolyte. (c) The acetate Faradaic Efficiency over $2Cu_{NP}$-Cu_1, Cu_{NP}-Cu_1 and $0.5Cu_{NP}$-Cu_1.

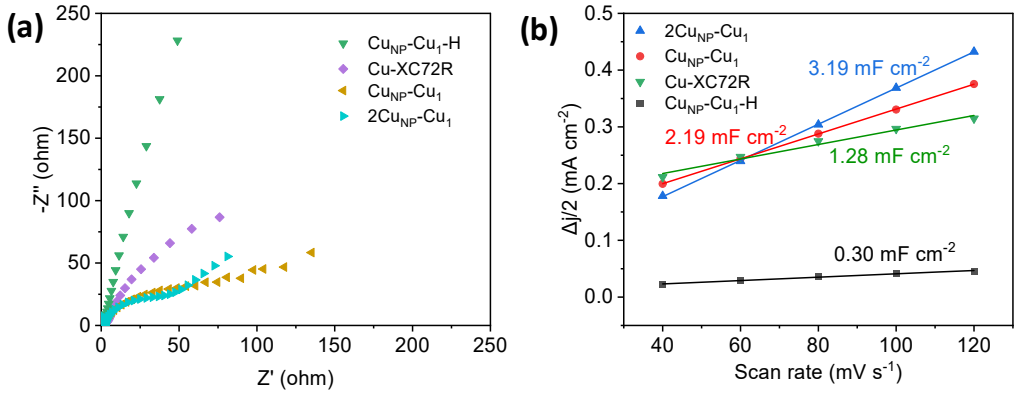

Fig. S14. (a) The electrochemical impedance spectroscopy, (b) Double-layer capacitance for Cu NPs, $2Cu_{NP}$-Cu_1, Cu_{NP}-Cu_1 and CuSA catalyst.

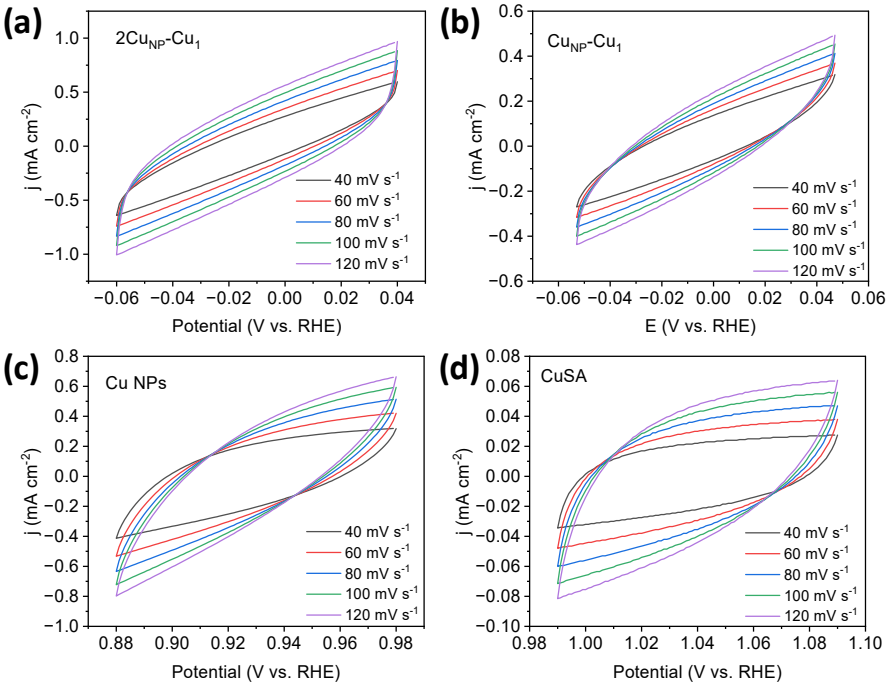

Fig. S15. Cyclic voltammograms with different scan rates (40, 60, 80, 100 and 120 mV s^{-1}) for (a) 2Cu$_{NP}$-Cu$_1$, (b) Cu$_{NP}$-Cu$_1$, (c) Cu NPs, (d) CuSA.

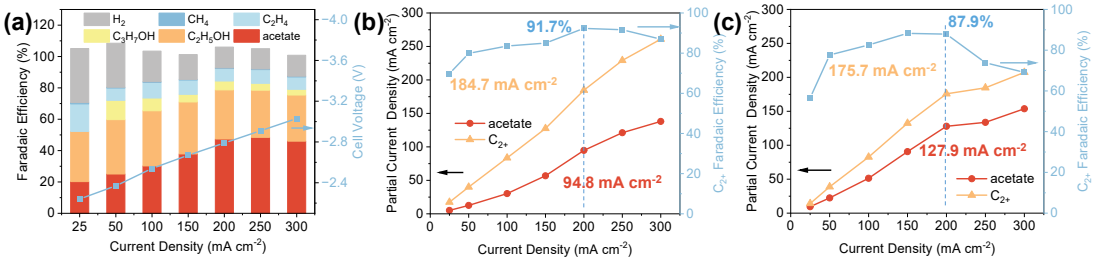

Fig. S16. (a) Faradaic efficiency of products and cell voltages for Cu_{NP}-Cu_1 catalyst at 0.1 MPa CO partial pressure in MEA electrolyzer. The C_{2+}/acetate partial current density and Faradaic efficiency of C_{2+} products at different potentials over (b) 0.1 and (c) 1.0 MPa in 1.0 M KOH electrolyte. The numbers represent C_{2+} Faradaic efficiency and current density under the total current density of 200 mA cm^{-2}.

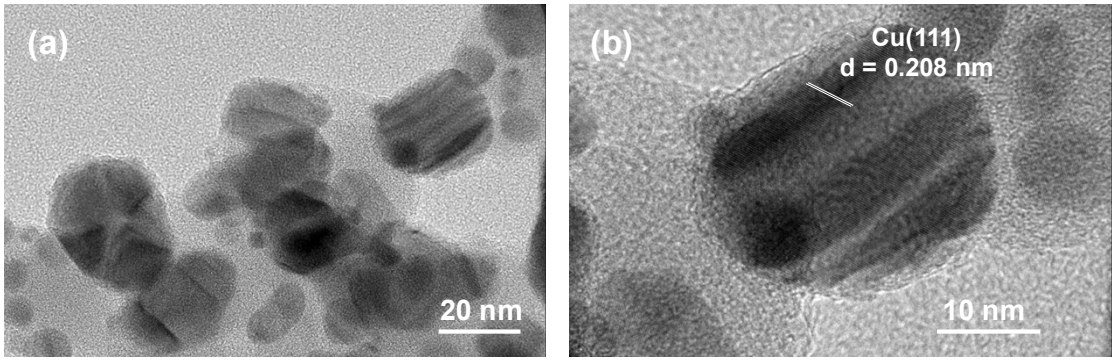

Fig. S17. TEM images of Cu_{NP}-Cu_1 after CO electrolysis at –1.24 V vs. RHE.

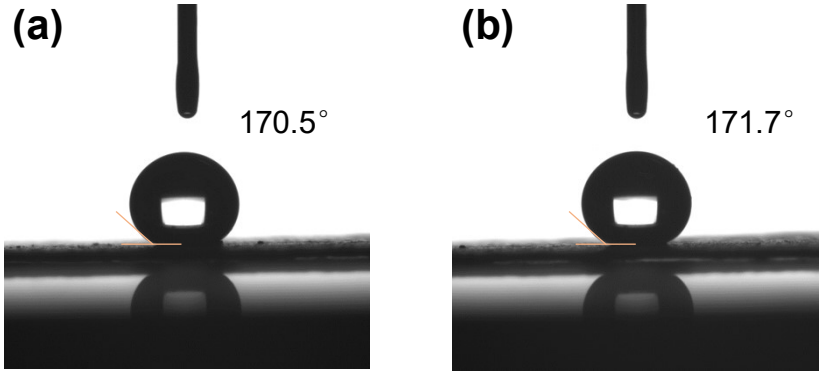

Fig. S18. Contact angle measurement on Cu_{NP}-Cu_1 (a) before and (b) after reaction.

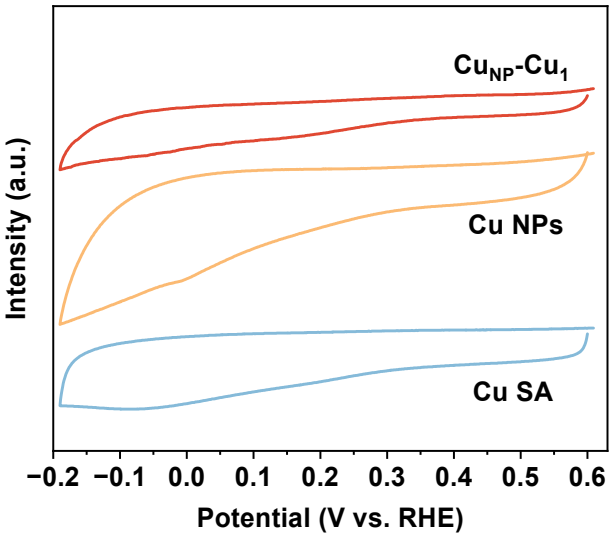

Fig. S19. Cyclic voltammetry tests of Cu_{NP}-Cu_1, Cu NPs and CuSA in 0.1 M K_2SO_4 electrolyte without CO.

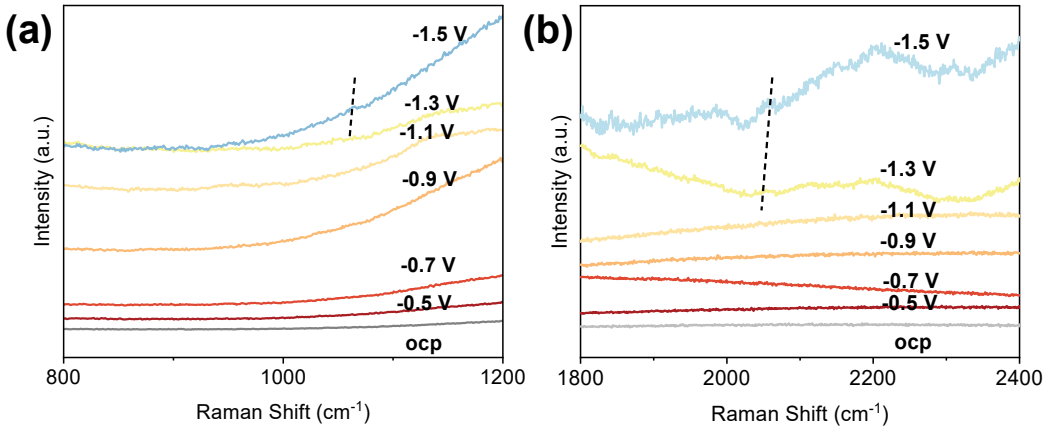

Fig. S20. *Operando* Raman spectra of Cu NPs catalyst.

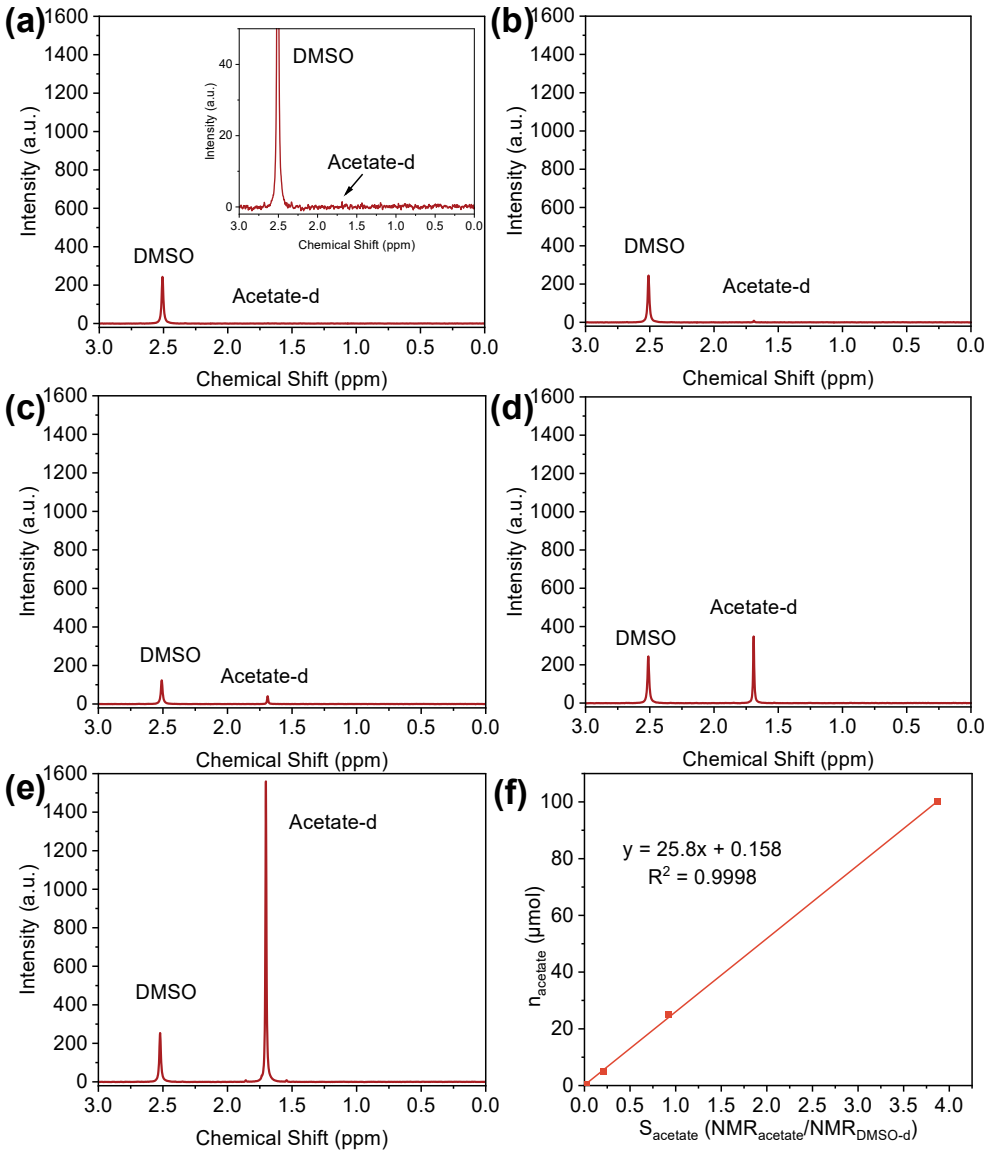

Fig. S21. NMR spectra of standard solution (dissolved in D_2O): (a) 0.1 μmol CD_3COOD + 14 μmol DMSO-d6, (b) 0.5 μmol CD_3COOD + 14 μmol DMSO-d6, (c) 5 μmol CD_3COOD + 14 μmol DMSO-d6, (d) 25 μmol CD_3COOD + 14 μmol DMSO-d6, (e) 100 μmol CD_3COOD + 14 μmol DMSO-d6. δ = 2.52 represents DMSO-d6 (hexadeuterodimethyl sulfoxide), δ = 1.70 represents acetate-d (CD_3COOD). (f) The concentration relationship of $n_{acetate}$ and $S_{acetate\text{-}d}$ ($NMR_{acetate}/NMR_{DMSO\text{-}d6}$).

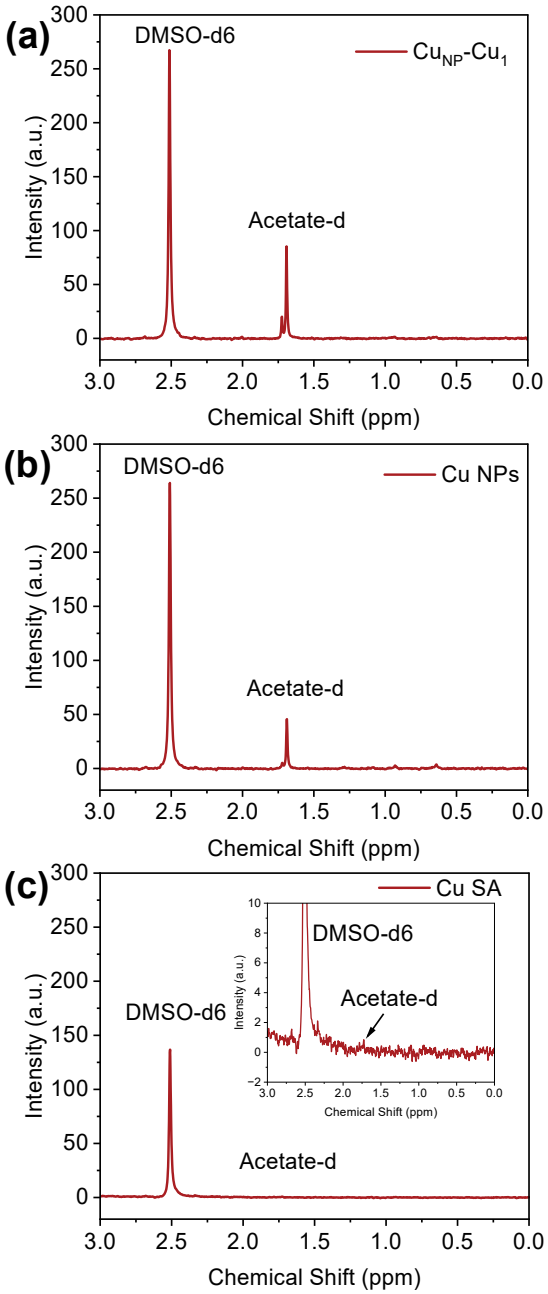

Fig. S22. NMR spectra of acetate-d derived from CO reduction in 1.0 M KOH solution (dissolved in D_2O): (a) Cu_{NP}-Cu_1, (b) Cu NPs, and (c) CuSA. δ = 2.51 represents DMSO-d6 (hexadeuterodimethyl sulfoxide), δ = 1.69 represents acetate-d (deuterated acetate).

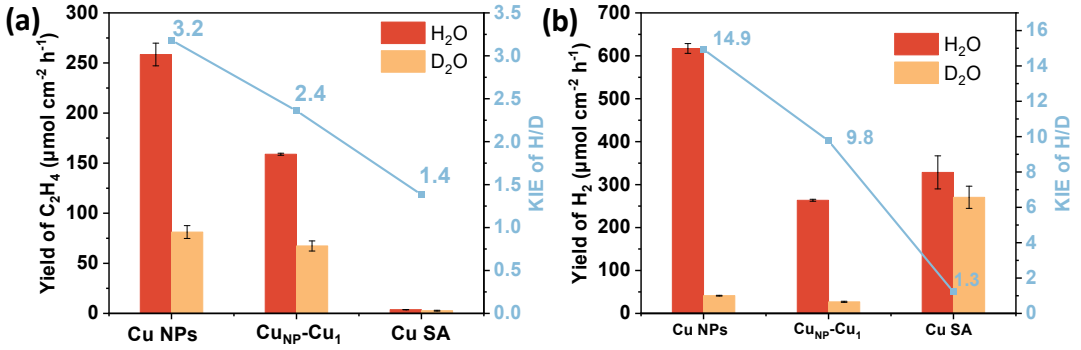

Fig. S23. (a) C_2H_4 yield and (b) H_2 yield of H_2O/D_2O on Cu NPs, Cu_{NP}-Cu_1 and CuSA catalysts in 1.0 M KOH electrolyte.

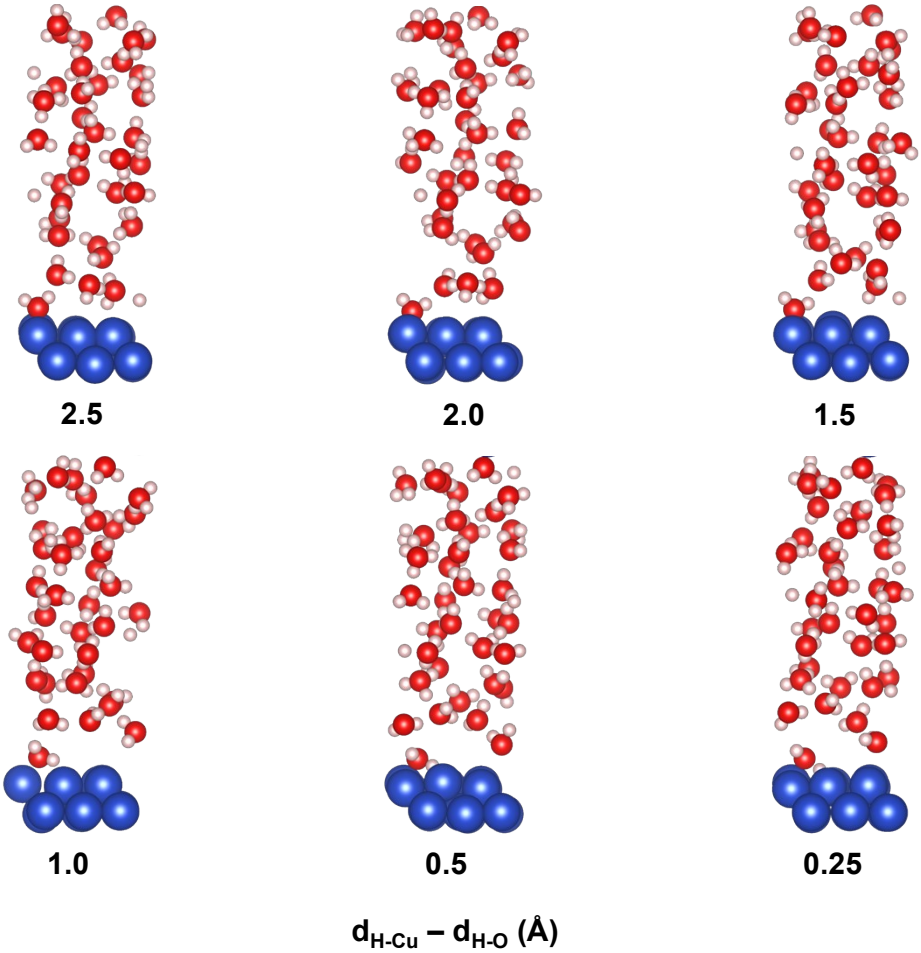

Fig. S24. Side view of DFT configurations for the initial state, transition states, and final state of the H_2O dissociation on Cu(100) at different Δ*d*. The number below model represents $\Delta d = d_{H\text{-}Cu} - d_{H\text{-}O}$. Color code: blue for copper, red for oxygen, pink for hydrogen.

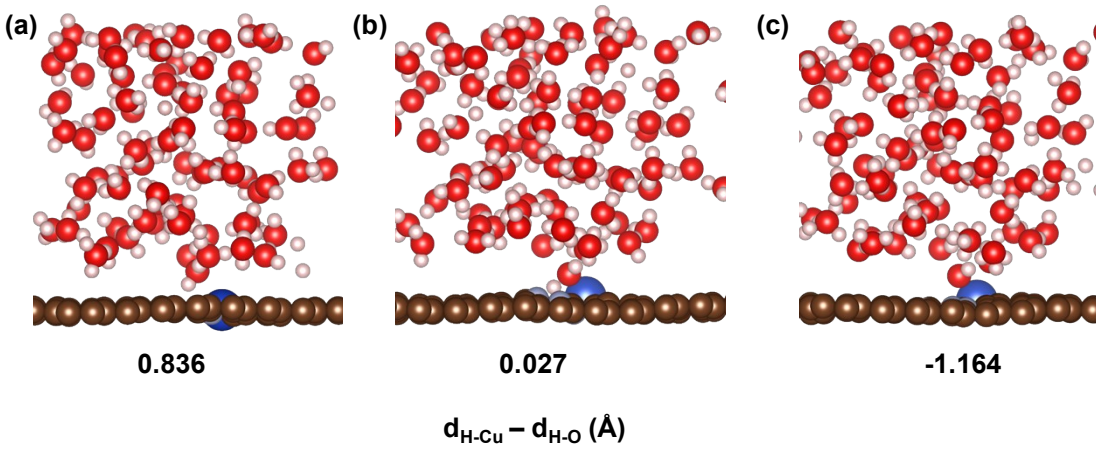

Fig. S25. Side view of DFT configurations for (a) the initial state, (b) transition state, and (c) final state of the H_2O dissociation on Cu-N_3 at different Δ*d*. The number below model represents $\Delta d = d_{H-N} - d_{H-O}$. Color code: blue for copper, red for oxygen, pink for hydrogen, gray for nitrogen.

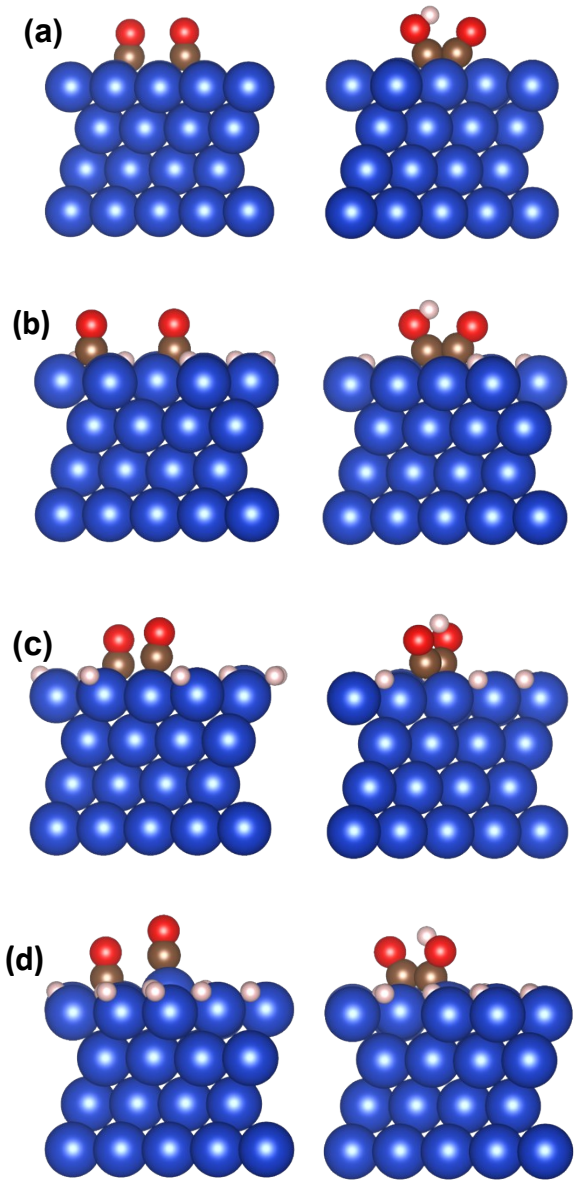

Fig. S26. Side view of DFT configurations for the initial state (left) and final state (right) of H coverage on Cu(111): (a) 0 ML, (b) 1/4 ML, (c) 1/2 ML, and (d) 3/4 ML.

Table S1. Structural parameters extracted from the EXAFS fitting.

Sample	Scattering	CN_{real}	R(Å)	σ^2 (10^{-3} Å^2)	ΔE_0 (eV)	*R* factor
Cu foil	Cu-Cu	12	2.54±0.003	8.6±0.4	4.00±0.56	0.0038
Cu_{NP}-Cu_1	Cu-Cu	5.0±0.6	2.53±0.01	8.8±1.2	2.45±1.61	0.0145
	Cu-N	2.7±0.3	1.93±0.01			

Note: s_0^2 is the amplitude reduction factor (s_0^2 = 0.8752); CN_{real} is the coordination number; *R* is interatomic distance (the bond length between central atoms and surrounding coordination atoms); σ^2 is Debye-Waller factor (a measure of thermal and static disorder in absorber-scatterer distances); ΔE_0 is edge-energy shift (the difference between the zero kinetic energy value of the sample and that of the theoretical model). *R* factor is used to value the goodness of the fitting.

Table S2. Cu_{NP}:Cu_1 atomic ratio determined by ICP-OES test

Sample	**wt.%**	**ratio Cu_{NP}/Cu_1**
CuSA	2.53	-
Cu_{NP}-Cu_1	14.26	82.3/17.7
2CuSA	2.18	-
$2Cu_{NP}$-Cu_1	23.74	90.8/9.2
0.5CuSA	2.2	
$0.5Cu_{NP}$-Cu_1	4.72	53.3/46.7

Table S3. Comparison of this work to prior reports in the CO electroreduction performance.

Catalyst	$FE_{acetate}$ (%)	$J_{acetate}$ (mA cm^{-2})	FE_{C2+} (%)	J_{C2+} (mA cm^{-2})	Stability (h)	Cell	Reference
Cu_{NP}-Cu_1	60.6	111.1	83.4	150.5	132	Flow cell	This work
Cu nanosheets	48	131	68.7	137.4	3	Flow cell	[11]
Micron-sized Cu	27	54	78.8	157.6	2	Flow cell	[12]
$Cu_{0.9}Ni_{0.1}$	47	93	76	150.3	3	Flow cell	[13]
N-doped CuF	42	180	65	278	1	Flow cell	[14]
Cu nanoflowers	35.7	0.04	84.6	0.42	10	H-cell	[15]
Fragmented Cu	~5	~2.5	~65	~32.5	3.3	Flow cell	[16]
Cu particle	~4	~0.6	~74	~11.0	24	H-cell	[17]
Cu nanocavity	7.8	0.6	62.3	4.9	2.5	Flow cell	[18]
Cu adparticle	4.8	2.4	80.8	40.4	0.7	Flow cell	[19]
Ag-doped Cu	4.7	0.6	73.6	3.5	3.3	Flow cell	[20]

Table S4. Reaction energy of *COCOH formation, *COCOH to *CCO and *COCOH to *COHCOH over Cu as a function of *H coverage.

***H coverage**	**Reaction energy (eV)**		
(ML)	**2*CO→*COCOH**	***COCOH→*COHCOH**	***COCOH→*CCO**
0	1.14	-0.61	-1.09
1/4	1.15	-0.61	-1.11
2/4	1.33	-0.49	-1.04
3/4	1.02	-0.41	-1.64

References

1. G. Kresse and J. Furthmüller, *Comp. Mater. Sci.*, 1996, **6**, 15-50.
2. G. Kresse and J. Furthmüller, *Phys. Rev. B*, 1996, **54**, 11169.
3. B. Hammer, L. B. Hansen and J. K. Nørskov, *Phys. Rev. B*, 1999, **59**, 7413.
4. Y. Zhang and W. Yang, *Phys. Rev. Lett.*, 1998, **80**, 890.
5. S. Grimme, *Journal of Computational Chemistry*, 2006, **27**, 1787-1799.
6. A. A. Peterson, F. Abild-Pedersen, F. Studt, J. Rossmeisl and J. K. Nørskov, *Energy & Environmental Science*, 2010, **3**, 1311-1315.
7. S. Nosé, *J. Comput. Chem.*, 1984, **81**, 511-519.
8. W. G. Hoover, *Phys. Rev. A*, 1985, **31**, 1695.
9. H. Oberhofer, C. Dellago and P. L. Geissler, *J Phys Chem B*, 2005, **109**, 6902-6915.
10. H.-M. Yan, Z. Zhang and Y.-G. Wang, *ACS Catal.*, 2024, **14**, 3596-3605.
11. W. Luc, X. Fu, J. Shi, J.-J. Lv, M. Jouny, B. H. Ko, Y. Xu, Q. Tu, X. Hu and J. Wu, *Nat. Catal.*, 2019, **2**, 423-430.
12. M. Jouny, W. Luc and F. Jiao, *Nat. Catal.*, 2018, **1**, 748-755.
13. C. Yang, B. H. Ko, S. Hwang, Z. Liu, Y. Yao, W. Luc, M. Cui, A. S. Malkani, T. Li and X. Wang, *Sci. Adv.*, 2020, **6**, eaaz6844.
14. F. Ni, H. Yang, Y. Wen, H. Bai, L. Zhang, C. Cui, S. Li, S. He, T. Cheng and B. Zhang, *Sci. China Mater.*, 2020, **63**, 2606-2612.
15. L. Wang, S. Nitopi, A. B. Wong, J. L. Snider, A. C. Nielander, C. G. Morales-Guio, M. Orazov, D. C. Higgins, C. Hahn and T. F. Jaramillo, *Nat. Catal.*, 2019, **2**, 702-708.
16. Y. Pang, J. Li, Z. Wang, C.-S. Tan, P.-L. Hsieh, T.-T. Zhuang, Z.-Q. Liang, C. Zou, X. Wang, P. De Luna, J. P. Edwards, Y. Xu, F. Li, C.-T. Dinh, M. Zhong, Y. Lou, D. Wu, L.-J. Chen, E. H. Sargent and D. Sinton, *Nat. Catal.*, 2019, **2**, 251-258.
17. R. Chen, H.-Y. Su, D. Liu, R. Huang, X. Meng, X. Cui, Z.-Q. Tian, D. H. Zhang and D. Deng, *Angew. Chem. Int. Ed.*, 2020, **59**, 154-160.
18. T.-T. Zhuang, Y. Pang, Z.-Q. Liang, Z. Wang, Y. Li, C.-S. Tan, J. Li, C. T. Dinh, P. De Luna, P.-L. Hsieh, T. Burdyny, H.-H. Li, M. Liu, Y. Wang, F. Li, A. Proppe, A. Johnston, D.-H. Nam, Z.-Y. Wu, Y.-R. Zheng, A. H. Ip, H. Tan, L.-J. Chen, S.-H. Yu, S. O. Kelley, D. Sinton and E. H. Sargent, *Nat. Catal.*, 2018, **1**, 946-951.
19. J. Li, F. Che, Y. Pang, C. Zou, J. Y. Howe, T. Burdyny, J. P. Edwards, Y. Wang, F. Li, Z. Wang, P. De Luna, C.-T. Dinh, T.-T. Zhuang, M. I. Saidaminov, S. Cheng, T. Wu, Y. Z. Finfrock, L. Ma, S.-H. Hsieh, Y.-S. Liu, G. A. Botton, W.-F. Pong, X. Du, J. Guo, T.-K. Sham, E. H. Sargent and D. Sinton, *Nat. Commun.*, 2018, **9**, 4614.
20. X. Wang, Z. Wang, T.-T. Zhuang, C.-T. Dinh, J. Li, D.-H. Nam, F. Li, C.-W. Huang, C.-S. Tan, Z. Chen, M. Chi, C. M. Gabardo, A. Seifitokaldani, P. Todorović, A. Proppe, Y. Pang, A. R. Kirmani, Y. Wang, A. H. Ip, L. J. Richter, B. Scheffel, A. Xu, S.-C. Lo, S. O. Kelley, D. Sinton and E. H. Sargent, *Nat. Commun.*, 2019, **10**, 5186.